THE JOURNAL OF PHYSICAL CHEMISTRY A

Article

Cite This: J. Phys. Chem. A 2018, 122, 3374−3382

pubs.acs.org/JPCA

Spin−Orbit Splittings and Low-Lying Electronic States of AuSi and AuGe: Anion Photoelectron Spectroscopy and *ab Initio* Calculations

Quoc Tri Tran,[†] Sheng-Jie Lu,[‡] Li-Juan Zhao,[§] Xi-Ling Xu,[‡,∥] Hong-Guang Xu,[‡,∥] Van Tan Tran,*[,†] Jun Li,*[,§] and Wei-Jun Zheng*[,‡,∥]

[†]Theoretical and Physical Chemistry Division, Dong Thap University, 783-Pham Huu Lau, Cao Lanh City, Ward 6, Dong Thap, Vietnam

[‡]Beijing National Laboratory for Molecular Sciences (BNLMS), State Key Laboratory of Molecular Reaction Dynamics, Institute of Chemistry, Chinese Academy of Sciences, Beijing 100190, China

[§]Department of Chemistry and Key Laboratory of Organic Optoelectronics and Molecular Engineering of Ministry of Education, Tsinghua University, Beijing 100084, China

[∥]University of Chinese Academy of Sciences, Beijing 100049, China

Supporting Information

ABSTRACT: We measured the photoelectron spectra of diatomic $AuSi^-$ and $AuGe^-$ and conducted calculations on the structures and electronic properties of $AuSi^{-/0}$ and $AuGe^{-/0}$. The calculations at the CASSCF/CASPT2 level confirmed that experimentally observed spectra features of $AuSi^-$ and $AuGe^-$ can be attributed to the transitions from the $^3\Sigma^-$ anionic ground state to the $^2\Pi$ ($^2\Pi_{1/2}$ and $^2\Pi_{3/2}$), $^4\Sigma^-$, $3^2\Sigma^+$, and $4^2\Sigma^+$ electronic states of their neutral counterparts. The electron affinities (EAs) of AuSi and AuGe are determined by the experiments to be 1.54 ± 0.05 and 1.51 ± 0.05 eV, respectively. The spin−orbit splittings ($^2\Pi_{1/2}$−$^2\Pi_{3/2}$) of AuSi and AuGe measured in this work are in agreement with the literature values. The energy difference between the $^4\Sigma^-$ (A) and $^2\Pi_{1/2}$ states of AuSi obtained in this work is in reasonable agreement with the literature value, while that of AuGe obtained in this work by anion photoelectron spectroscopy is slightly larger than the literature value by neutral emission spectroscopy. The term energies of the $3^2\Sigma^+$ (B) and $4^2\Sigma^+$ (C) states of AuSi and AuGe were also determined based on the photoelectron spectra. Because of the different bond lengths between the anionic and neutral states, the electronic state terms energies of AuSi and AuGe estimated from the anion photoelectron spectra might be slightly different from those obtained from the neutral emission spectra.

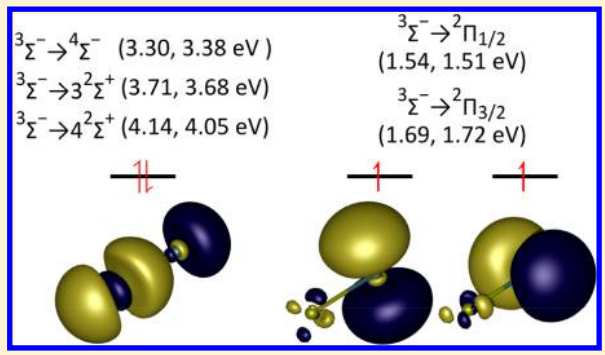

1. INTRODUCTION

The Au−Si and Au−Ge alloys are important in fabrication of microelectronics, microsensors, and new nanomaterials.[1−8] Understanding the structures and electronic properties of Au-doped semiconductor clusters may provide useful information for the development of semiconductor nanomaterials and for their potential applications in industry. The structures of Au-doped silicon clusters[9−12] and Au-doped germanium clusters[13−18] were studied previously by many calculations. The vibrational frequencies and structures of $AuSi_n^+$ (n = 2−11, 14, 15) were investigated by infrared multiphoton dissociation (IRMPD) experiment.[19] The electronic states and bonding properties of $SiAu_4^-$, $Si_2Au_n^-$ (n = 2, 4), $Si_3Au_3^-$, and $AuSi_n^-$ (n = 4−12) were explored with size-selected photoelectron spectroscopy experiments.[20−23] The electronic states and structures of $AuGe_n^-$ (n = 2−12) clusters were also investigated by size-selected photoelectron spectroscopy in combination with *ab initio* calculations.[24] The Au-doped Group 14 cluster ions such as $[Au_3Ge_{18}]^{5-}$, $[Au_3Ge_{45}]^{9-}$, and $[AuGe_{18}(Si(SiMe_3)_3)_6]^-$ were synthesized in solutions and characterized by a number of techniques.[25−27]

Regarding diatomic AuSi and AuGe molecules, the emission spectra of AuSi and AuGe were measured by Barrow[28] and by Houdart and Schamps.[29] The results proposed a ground state of $^2\Pi_{1/2}$ with a spin−orbit splitting from $^2\Pi_{1/2}$ to $^2\Pi_{3/2}$ of 1071 cm^{-1} for AuSi and of 1552 cm^{-1} for AuGe. The dissociation energy of AuSi was measured using Knudsen cell mass spectrometer.[30] The rotational constant of AuSi was determined based on the near-infrared bands.[31] The rovibronic bands of AuSi were measured with cavity ringdown laser absorption spectroscopy.[32] The low-lying states of AuSi, $AuSi^+$, and $AuSi^-$ were studied by the multiconfigurational CASSCF/CASPT2 calculations.[12,33] The ground states of AuSi, $AuSi^+$, and $AuSi^-$ were predicted to be $^2\Pi$, $^1\Sigma^+$, and $^3\Sigma^-$.[12] Also, the ground state of AuSi was computed to be the $^2\Pi_{1/2}$ state, and

Received: February 7, 2018
Revised: March 15, 2018
Published: March 19, 2018

DOI: 10.1021/acs.jpca.8b01366
J. Phys. Chem. A 2018, 122, 3374−3382

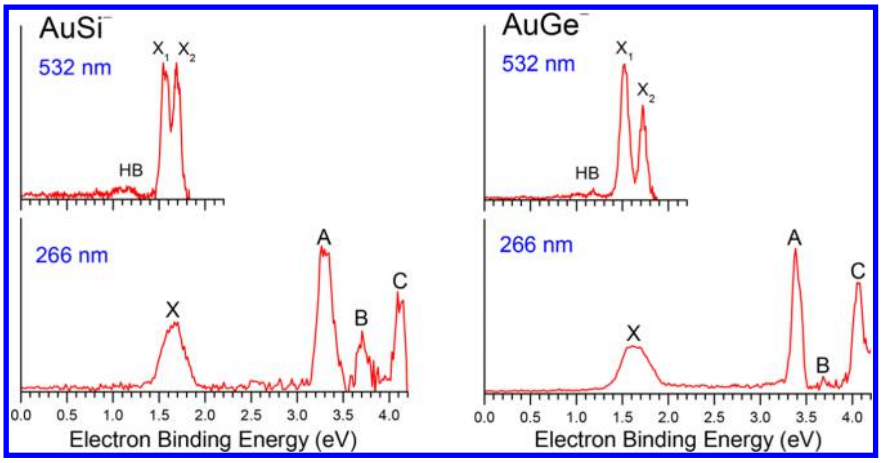

Figure 1. Photoelectron spectra of $AuSi^-$ and $AuGe^-$ recorded with 532 and 266 nm photons.

the spin−orbit splitting from $^2\Pi_{1/2}$ to $^2\Pi_{3/2}$ was evaluated to be 1527 cm^{-1}.[33] These computed results were in agreement with the emission spectra of AuSi.[28,29] However, the spin−orbit splitting predicted by theory is slightly larger than the experimental value. To best of our knowledge, there is no quantum chemical calculation on the low-lying states of $AuGe^-$ and AuGe.

In order to give a deeper understanding of the low-lying electronic states of $AuSi^{-/0}$ and $AuGe^{-/0}$, we investigate the electronic structures of $AuSi^{-/0}$ and $AuGe^{-/0}$ by anion photoelectron spectroscopy and quantum chemical calculations. By measuring the electron detachment energies of the anion, anion photoelectron spectroscopy can give relative energies of all the relevant low-lying electronic states of the neutral molecule that have not been recorded in the emission spectra of AuSi and AuGe. Also, the spin−orbit splitting energies of the low-lying electronic states of AuSi and AuGe are determined by anion photoelectron spectroscopy. Moreover, the structural variations from the initial anionic state to the final neutral state within an electron detachment process are recorded as vibrational progressions in the spectrum. Otherwise, the *ab initio* calculations with density functional theory (DFT) and CASSCF/CASPT2 method are carried out to provide the potential energy profiles, relative energies, spin−orbit splitting energies, vibrational frequencies, and bond distances of the relevant electronic states of $AuSi^{-/0}$ and $AuGe^{-/0}$. The electron detachment energies of the anion are calculated and the Franck−Condon factors of the transitions from the anionic state to the neutral states are simulated. The computed results are used to interpret the photoelectron spectra of $AuSi^-$ and $AuGe^-$.

2. EXPERIMENTAL AND COMPUTATIONAL METHODS

2.A. Experimental Methods. The experiments were conducted on a home-built apparatus consisting of a laser vaporization cluster source, a time-of-flight mass spectrometer, and a magnetic-bottle photoelectron spectrometer, which has been described elsewhere.[34] The $AuSi^-$ anions were generated in the laser vaporization source by laser ablation of a rotating and translating isotopically enriched Au/^{28}Si mixture disk target (13 mm diameter, Au:^{28}Si mole ratio 1:1, ^{28}Si (99.989%)) with the second harmonic (532 nm) light pulses from a Nd:YAG laser (Continuum Surelite II-10), while helium gas with ∼0.4 MPa backing pressure was allowed to expand through a pulsed valve (General Valve Series 9) into the source to cool the $AuSi^-$ anions. Similarly, the $AuGe^-$ anions were generated by laser ablation of a rotating and translating Au/Ge mixture disk target (Au:Ge mole ratio 1:1). The $AuSi^-$ and $AuGe^-$ anions were each size-selected with a mass gate, decelerated by a momentum decelerator before crossing with the beam of another Nd:YAG laser (Continuum Surelite II-10, 532, 355, and 266 nm) at the photodetachment region. The photoelectrons were energy-analyzed by the magnetic-bottle photoelectron spectrometer. The photoelectron spectra were calibrated with the spectra of Bi^-, Cs^-, Cu^-, and Au^- ions taken at similar conditions. The resolution of the magnetic-bottle photoelectron spectrometer was about 40 meV at electron kinetic energy of 1 eV.

2.B. Computational Methods. The nonrelativistic (NR), scalar relativistic (SR), and spin−orbit (SO) energy levels of AuSi and AuGe are obtained using the Amsterdam Density Functional software (ADF, 2016.10)[35−37] with the B3LYP[38−41] method and TZP basis sets.[42] The frozen core approximation was also employed with [$1s^2$−$4d^{10}$] for Au, [$1s^2$−$2p^6$] for Si, and [$1s^2$−$3p^6$] for Ge. In order to better understand the bonding properties of $AuSi^-$ and $AuGe^-$, the NBO analysis was also performed.

The low-lying states of $AuSi^{-/0}$ and $AuGe^{-/0}$ was investigated with the CASSCF/CASPT2 method. The $AuSi^{-/0}$ and $AuGe^{-/0}$ have $C_{\infty v}$ symmetry. Because only Abelian point groups are supported in MOLCAS, all the CASSCF/CASPT2 calculations were performed in C_{2v} symmetry. The triple-ζ ANO-RCC basis sets with contraction schemes of [24s21p15d11f4g2h]/(8s6p5d3f2g) for Au, [17s12p5d4f2g]/(5s4p2d1f) for Si, and [20s17p11d5f2g]/(6s5p3d2f1g) for Ge were used.[43,44] The scalar relativistic effects were treated with the second-order Douglas-Kroll Hamiltonian.[45−47] To reduce the memory for storing two-electron integrals, Cholesky decomposition with an accuracy of 10^{-6} au were employed.[48−50] In the CASPT2 step, an imaginary shift of 0.1 was applied to prevent the intruder states. Also, the default IPEA shift of 0.25 was used in the CASPT2 calculations. The wave function for CASPT2 was obtained from a CASSCF calculation. The previous study on the electronic structures of AuSi uses an active space of 10 orbitals which includes the 5d and 6s of Au and the 3s and 3p of Si.[33] In this work, our CASSCF/CASPT2 calculations employ the same active space for $AuSi^{-/0}$ and $AuGe^{-/0}$. In particular, for $AuGe^{-/0}$, the 4s and 4p of Ge were included in the active space instead of the 3s and 3p of Si. Overall, the active spaces for $AuSi^{-/0}$ and $AuGe^{-/0}$ consist of 15 or 16

DOI: 10.1021/acs.jpca.8b01366
J. Phys. Chem. A 2018, 122, 3374−3382

Table 1. Experimental VDEs of the Peaks Observed in the Photoelectron Spectra of $AuSi^-$ and $AuGe^-$ [a]

	VDE (eV)				
	X				
	X_1	X_2	A	B	C
$AuSi^-$	1.54 (5)	1.69 (5)	3.30 (8)	3.71 (8)	4.14 (8)
$AuGe^-$	1.51 (5)	1.72 (5)	3.38 (8)	3.68 (8)	4.05 (8)
assignment	$^3\Sigma^- \rightarrow {}^2\Pi_{1/2}$	$^3\Sigma^- \rightarrow {}^2\Pi_{3/2}$	$^3\Sigma^- \rightarrow {}^4\Sigma^-$	$^3\Sigma^- \rightarrow 3^2\Sigma^+$	$^3\Sigma^- \rightarrow 4^2\Sigma^+$

[a]The numbers in the parentheses indicate the uncertainties of the last digits.

electrons distributed in 10 orbitals. After spin-free CASSCF/CASPT2 calculations, spin−orbit state interactions were carried out with the atomic mean field approximation.[51] All the CASSCF/CASPT2 calculations were carried out with MOLCAS@UU 8.0.[52]

3. EXPERIMENTAL RESULTS

The photoelectron spectra of $AuSi^-$ and $AuGe^-$ anions recorded with 532 and 266 nm photons are shown in Figure 1. (The spectra recorded with 355 nm photons are shown in the Supporting Information.) The vertical detachment energies (VDEs) of these clusters obtained from the photoelectron spectra are reported in Table 1. It is worth noting that the original photoelectron spectrum of $AuSi^-$ at 266 nm was contaminated by the signals of Si_8^- because the ion intensity of $AuSi^-$ was very weak and it was always disturbed by the strong ion intensity of Si_8^-. Thus, the 266 nm spectrum of $AuSi^-$ anion displayed in Figure 1 is obtained by subtracting the photoelectron signals of Si_8^- from the original spectrum. (The detailed information about the spectrum subtraction can be found in the Supporting Information.)

The 266 nm spectrum of $AuSi^-$ reveals a broad peak (X) centered at 1.66 eV, and three sharp peaks A, B, and C at 3.30, 3.71, and 4.14 eV, respectively. In the 532 nm spectrum of $AuSi^-$, the X peak is resolved into two peaks centered at 1.54 (X_1) and 1.69 eV (X_2) because the instrumental resolution for that region is better at 532 nm than at 266 nm. The X_1 and X_2 more likely correspond to the transitions from the ground state of $AuSi^-$ anion to the spin−orbital splitting states of AuSi neutral. In addition, a weak broad feature in the range of 0.8−1.2 eV can be observed in the 532 nm spectra of $AuSi^-$, which is assigned as a hot band (HB) due to the transition from the vibrational excited state of $AuSi^-$ anion to the spin−orbital splitting states of AuSi neutral.

The 266 nm spectrum of $AuGe^-$ shows a broad peak (X) centered at 1.63 eV, followed by a high-intensity sharp peak (A) at 3.38 eV, a weak peak (B) at 3.68, and an additional high-intensity sharp peak (C) at 4.05 eV. The broad X peak is resolved into two peaks (X_1, X_2) centered at 1.51 and 1.72 eV in the 532 nm spectrum. Also, a weak low binding energy hot band (HB) in the range of 1.0−1.4 eV can be observed the 532 nm spectrum of $AuGe^-$, which has been confirmed by variations of the hot band intensity at different experimental conditions.

4. COMPUTATIONAL RESULTS

The NR, SR, and SO energy level of AuSi are shown in Figure 2. The NR, SR, and SO energy levels of AuGe are shown in Figure 3. For AuSi, the 6s atomic orbital (AO) of Au ($sd^{0.12}$) interacts with the 3p AOs of Si ($sp^{21.29}d^{0.22}$) forming one bonding orbital (3σ, 65% Au and 35% Si) and one antibonding orbital (4σ, 35% Au and 65% Si), while the 5d AOs of Au split

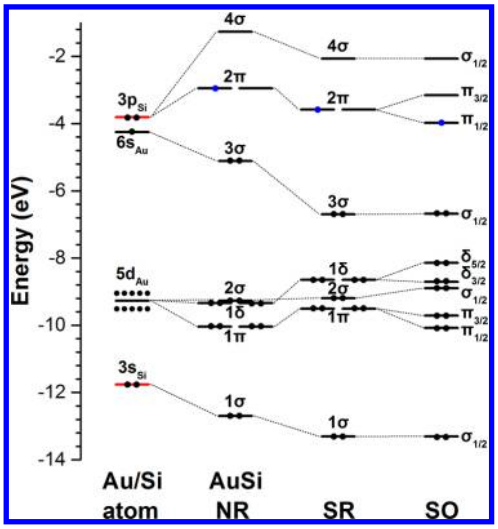

Figure 2. Nonrelativistic (NR), scalar relativistic (SR), and spin−orbit (SO) energy levels of AuSi.

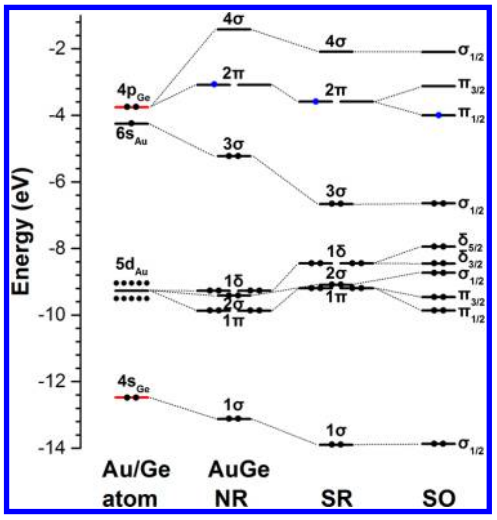

Figure 3. Nonrelativistic (NR), scalar relativistic (SR), and spin−orbit (SO) energy levels of AuGe.

into five molecular orbitals. For AuGe, the 6s AO of Au ($sd^{0.12}$) bonds with the 4p AOs of Ge ($sp^{26.89}d^{0.22}$) forming one 3σ bonding orbital (65% Au and 35% Si) and one 4σ antibonding orbital (35% Au and 65% Si), leaving the 5d AOs of Au splitting into five molecular orbitals without interacting with Ge.

4.A. $AuSi^-$ and AuSi. The CASSCF/CASPT2 potential energy curves of the low-lying states of $AuSi^-$ and AuSi are presented in Figure 4, parts a and b. The Au−Si bond distances, harmonic vibrational frequencies, and relative energies of the low-lying states of $AuSi^-$ and AuSi as defined from the potential

DOI: 10.1021/acs.jpca.8b01366
J. Phys. Chem. A 2018, 122, 3374−3382

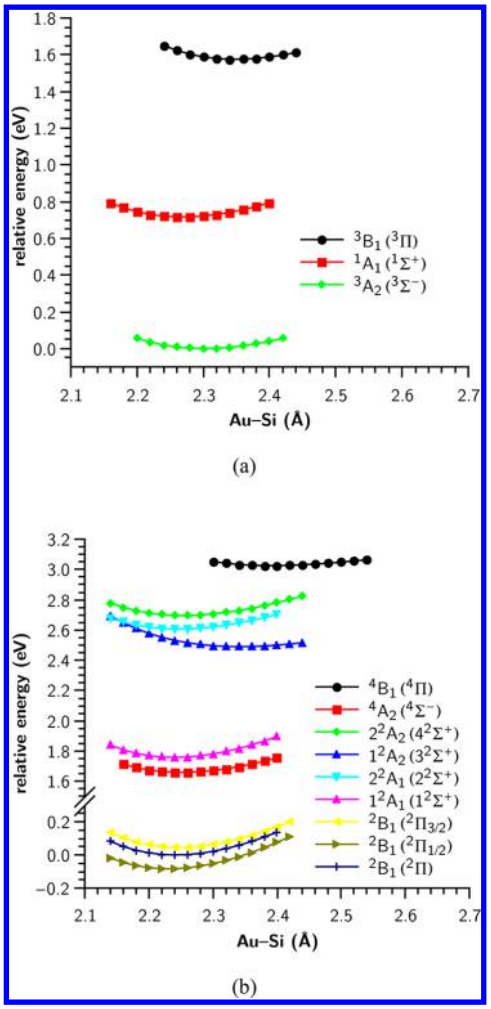

Figure 4. Potential energy curves of the low-lying states of $AuSi^-$ (a) and of AuSi (b) as obtained from CASPT2 calculations.

energy curves are collected in the upper part of Table 2. The calculated results show that the ground state of $AuSi^-$ is a $^3\Sigma^-$ with a bond distance of 2.031 Å and a harmonic vibrational frequency of 322 cm^{-1}. The qualitative molecular orbital diagram of the $^3\Sigma^-$ as presented in Figure 5 shows that the $11b_1$ (π) and $11b_2$ (π) orbital are singly occupied. These two orbitals are predominantly $3p_x$ and $3p_y$ of Si. All the predominantly 5d and 6s of Au orbitals ($20a_1$, $21a_1$, $22a_1$, $10b_1$, $10b_2$, and $4a_1$) are fully occupied. On the other hand, the ground state of the AuSi is a $^2\Pi$ with a bond distance of 2.241 Å and a vibrational frequency of 389 cm^{-1}. In the spin–orbit state interaction calculations, the $^2\Pi$ is split into the $^2\Pi_{1/2}$ and $^2\Pi_{3/2}$ in which the $^2\Pi_{1/2}$ is the ground state. The spin–orbit splitting of the $^2\Pi_{1/2}$ and $^2\Pi_{3/2}$ is calculated to be 0.12 eV, in reasonable agreement with the experimental value of 0.15 ± 0.02 eV (1210 ± 160 cm^{-1}) in this work. The ground states of the anionic and neutral AuSi as obtained with the CASPT2 method in this work are in agreement with the previous results.[12,33]

The photoelectron spectra of $AuSi^-$ can be interpreted by electron detachments from the $^3\Sigma^-$ anionic ground state. The X band at 1.66 eV in the 266 nm spectrum is ascribed to the $^3\Sigma^-$ → $^2\Pi$ transition in which one electron from the $11b_2$ (π) orbital is detached. The vertical detachment energy (VDE) as computed with the CASPT2 method is 1.48 eV. Because of the spin–orbit interaction in the $^2\Pi$, the X band is split into the X_1 and X_2 bands centered at 1.54 and 1.69 eV in the 532 nm spectrum. The VDEs of the transitions from the $^3\Sigma^-$ to the $^2\Pi_{1/2}$ and to the $^2\Pi_{3/2}$ are calculated by theory to be 1.40 and 1.52 eV, respectively. On the other hand, the A, B, and C bands at 3.30, 3.71, and 4.14 eV in the 266 nm spectrum are assigned to the transitions from the $^3\Sigma^-$ to the $^4\Sigma^-$, $3^2\Sigma^+$, and $4^2\Sigma^+$ in which one electron is removed from the $22a_1$ (σ) orbital. The VDEs of these three transitions as computed with the CASPT2 method are 3.13, 3.96, and 4.17 eV, respectively. In general, we can say that all the calculated VDEs correspond well with the positions of the X (X_1 and X_2), A, B, and C bands in the experimental spectra.

The Franck–Condon factor simulation results for the $^3\Sigma^-$→ $^2\Pi_{1/2}$ and $^3\Sigma^-$ → $^2\Pi_{3/2}$ transitions are presented in Figure 6a and 6b. As can be seen from these figures, the $^3\Sigma^-$ → $^2\Pi_{1/2}$ and $^3\Sigma^-$→ $^2\Pi_{3/2}$ transitions have vibrational progressions of three or four peaks. The vibrational frequencies of the vibrational progression in the transition to $^2\Pi_{1/2}$ and to $^2\Pi_{3/2}$ are 395 and 386 cm^{-1}, respectively. These vibrational frequencies are too small to be observed in the 532 nm photoelectron spectrum. Indeed, in the 532 nm photoelectron spectrum of $AuSi^-$, the X_1 and X_2 bands appear with unresolved vibrational progressions. The vibrational progressions in the $^3\Sigma^-$→ $^2\Pi_{1/2}$ and $^3\Sigma^-$→ $^2\Pi_{3/2}$ transitions are the results of the detachment of one electron from the $11b_2$ (π) orbital of the $^3\Sigma^-$. As can be seen in Figure 3, the $11b_2$ (π) is a slightly antibonding orbital. The removal of one electron from an antibonding orbital would result in a decrease of the bond distance. Indeed, in the $^3\Sigma^-$→ $^2\Pi_{1/2}$ and $^3\Sigma^-$→ $^2\Pi_{3/2}$ transitions, the Ai-Si distances are reduced from 2.301 to 2.230 and to 2.248 Å. Overall, we can say that the decrease of Au–Si distance is the reason to why vibrational progressions appear in the $^3\Sigma^-$→ $^2\Pi_{1/2}$ and $^3\Sigma^-$→ $^2\Pi_{3/2}$ transitions.

4.B. $AuGe^-$ and AuGe. The potential energy curves of the low-lying states of $AuGe^-$ and AuGe as computed with the CASSCF/CASPT2 method are displayed in Figure 7, parts a and b. On the basis of the potential energy curves, the Au–Ge bond distance, harmonic vibrational frequency, and relative energy of these states are evaluated and the results are presented in the lower part of Table 2. It can be seen from Figure 7 and Table 2 that the ground states of the $AuGe^-$ and AuGe are similar to those of $AuSi^-$ and AuSi. For $AuGe^-$, the $^3\Sigma^-$ is calculated as the ground state with a bond distance of 2.378 Å and a vibrational frequency of 209 cm^{-1}. The molecular orbital diagram of the $^3\Sigma^-$ as presented in Figure 8 shows that the $13b_1$ (π) and $13b_2$ (π) are singly occupied. From Figure 8, we can see that the $13b_1$ and $13b_2$ are the $4p_x$ and $4p_y$ of Ge. Additionally, all the 5d and 6s of Au ($24a_1$, $25a_1$, $26a_1$, $12b_1$, $12b_2$, and $2a_2$) are fully occupied. Otherwise, the ground state of AuGe is a $^2\Pi$ state. The bond distance and vibrational frequency of the $^2\Pi$ as computed at CASPT2 level are 2.306 Å and 258 cm^{-1}. In the CASPT2 spin–orbit coupling calculations, the $^2\Pi$ is split into the $^2\Pi_{1/2}$ and $^2\Pi_{3/2}$. In these two doublet states, the $^2\Pi_{1/2}$ is the neutral ground state, while the $^2\Pi_{3/2}$ is 0.17 eV above. This result confirms the spin–orbit splitting of 0.21 ± 0.02 eV (1690 ± 160 cm^{-1}) estimated from the 532 nm photoelectron spectrum.

The photoelectron spectra of $AuGe^-$ are explained by the one-electron detachment processes from the $^3\Sigma^-$ anionic ground state. The X band at 1.63 eV in the 266 nm spectrum is attributed to the $^3\Sigma^-$ → $^2\Pi$ transition in which one electron from the $13b_2$ (π) orbital is detached. The VDE of this

DOI: 10.1021/acs.jpca.8b01366
J. Phys. Chem. A 2018, 122, 3374–3382

Table 2. Bond distances, vibrational frequencies, relative energies of the low-lying states of $AuSi^{-/0}$ and $AuGe^{-/0}$ and the adiabatic and vertical detachment energies (ADEs and VDEs) of the anion

						ADE (eV)	VDE (eV)	
cluster	state	leading configuration	R (Å)	freq (cm^{-1})	RE[b] (eV)	CASPT2	CASPT2	expt
$AuSi^-$	$^3A_2$ ($^3\Sigma^-$)	$22a_1^2 23a_1^0 11b_1^1 11b_2^1 4a_2^2$	2.301	322	0.00			
	$^1A_1$ ($^1\Sigma^+$)	$22a_1^2 23a_1^0 11b_1^2 11b_2^0 4a_2^2$	2.268	350	0.72			
	$^3B_1$ ($^3\Pi$)	$22a_1^2 23a_1^1 11b_1^1 11b_2^0 4a_2^2$	2.347	343	1.58			
AuSi	$^2B_1$ ($^2\Pi$)	$22a_1^2 23a_1^0 11b_1^1 11b_2^0 4a_2^2$	2.241	389	0.00 (1.46)	1.46	1.48	1.66, X
	$^2B_1$ ($^2\Pi_{1/2}$)[a]		2.230	395	−0.09 (1.37)	1.37	1.40	1.54, X_1
	$^2B_1$ ($^2\Pi_{3/2}$)[a]		2.248	386	0.04 (1.50)	1.50	1.52	1.69, X_2
	1^2A_1 ($1^2\Sigma^+$)	$22a_1^2 23a_1^1 11b_1^0 11b_2^0 4a_2^2$	2.240	392	1.76 (3.22)			
	2^2A_1 ($2^2\Sigma^+$)	$22a_1^1 23a_1^0 11b_1^2 11b_2^0 4a_2^2$	2.246	346	2.60 (4.06)			
	$^4A_2$ ($^4\Sigma^-$)	$22a_1^1 23a_1^0 11b_1^1 11b_2^1 4a_2^2$	2.251	351	1.66 (3.12)	3.12	3.13	3.30, A
	1^2A_2 ($3^2\Sigma^+$)	$22a_1^1 23a_1^0 11b_1^1 11b_2^1 4a_2^2$	2.342	271	2.49 (3.95)	3.95	3.96	3.71, B
	2^2A_2 ($4^2\Sigma^+$)	$22a_1^1 23a_1^0 11b_1^1 11b_2^1 4a_2^2$	2.254	339	2.69 (4.15)	4.15	4.17	4.14, C
	$^4B_1$ ($^4\Pi$)	$22a_1^1 23a_1^1 11b_1^1 11b_2^0 4a_2^2$	2.391	242	3.02 (4.48)			
$AuGe^-$	$^3A_2$ ($^3\Sigma^-$)	$26a_1^2 27a_1^0 13b_1^1 13b_2^1 5a_2^2$	2.378	209	0.00			
	$^1A_1$ ($^1\Sigma^+$)	$26a_1^2 27a_1^0 13b_1^2 13b_2^0 5a_2^2$	2.333	230	0.90			
	$^3B_1$ ($^3\Pi$)	$26a_1^2 27a_1^1 13b_1^1 13b_2^0 5a_2^2$	2.362	228	1.47			
AuGe	$^2B_1$ ($^2\Pi$)	$26a_1^2 27a_1^0 13b_1^1 13b_2^0 5a_2^2$	2.306	258	0.00 (1.36)	1.36	1.39	1.63, X
	$^2B_1$ ($^2\Pi_{1/2}$)[a]		2.320	264	−0.10 (1.26)	1.26	1.28	1.51, X_1
	$^2B_1$ ($^2\Pi_{3/2}$)[a]		2.337	278	0.08 (1.44)	1.44	1.45	1.72, X_2
	1^2A_1 ($1^2\Sigma^+$)	$26a_1^2 27a_1^1 13b_1^0 13b_2^0 5a_2^2$	2.311	251	1.80 (3.16)			
	2^2A_1 ($2^2\Sigma^+$)	$26a_1^1 27a_1^0 13b_1^2 13b_2^0 5a_2^2$	2.331	215	2.79 (4.15)			
	$^4A_2$ ($^4\Sigma^-$)	$26a_1^1 27a_1^0 13b_1^1 13b_2^1 5a_2^2$	2.330	223	1.76 (3.12)	3.12	3.13	3.38, A
	1^2A_2 ($3^2\Sigma^+$)	$26a_1^1 27a_1^0 13b_1^1 13b_2^1 5a_2^2$	2.430	172	2.44 (3.80)		3.80	3.68, B
	2^2A_2 ($4^2\Sigma^+$)	$26a_1^1 27a_1^0 13b_1^1 13b_2^1 5a_2^2$	2.331	217	2.87 (4.23)	4.23	4.23	4.05, C
	$^4B_1$ ($^4\Pi$)	$26a_1^1 27a_1^1 13b_1^1 13b_2^0 5a_2^2$	2.525	111	2.99 (4.35)			

[a]The spin−orbit coupling is calculated with four roots for each of the $^2B_1$, $^2B_2$, $^2A_1$, $^2A_2$, $^4A_2$, and $^4B_1$ states of the AuSi and AuGe. [b]The numbers in parentheses are relative energies as compared to the $^3A_2$ ($^3\Sigma^-$).

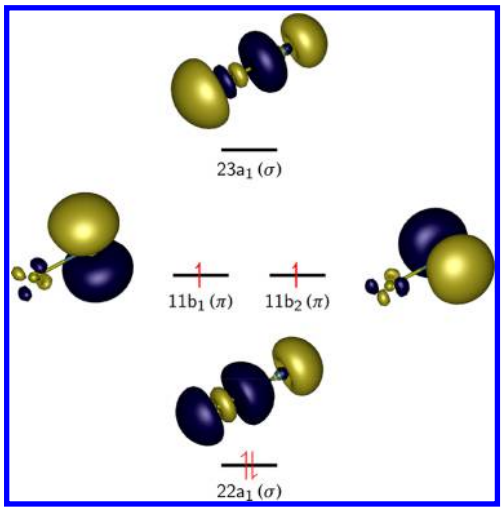

Figure 5. Qualitative molecular orbital diagram of the $^3A_2$ ($^3\Sigma^-$) of $AuSi^-$. The Au atom is placed on the left-hand side of the molecule.

transition as calculated at the CASPT2 level is 1.39 eV. Because of the spin−orbit coupling, the $^2\Pi$ is split into the $^2\Pi_{1/2}$ and $^2\Pi_{3/2}$. The computed VDEs of the transitions from the $^3\Sigma^-$ to the $^2\Pi_{1/2}$ and $^2\Pi_{3/2}$ are 1.28 and 1.45 eV. It can be seen that these computed VDEs are lightly lower than the experimental values of 1.51 and 1.72 eV in the experimental spectrum. Otherwise, the A, B, and C bands at 3.38, 3.68, and 4.05 eV in the experimental spectrum are the results of the transitions from the $^3\Sigma^-$ to the $^4\Sigma^-$, $3^2\Sigma^+$, and $4^2\Sigma^+$ states. In these transitions, one electron from the $26a_1$ orbital of the $^3\Sigma^-$ is detached. The calculated VDEs of these transitions are 3.13, 3.80, and 4.23 eV, respectively.

Figure 9a and 9b represent the Franck−Condon factor simulations for the $^3\Sigma^- \rightarrow {}^2\Pi_{1/2}$ and $^3\Sigma^- \rightarrow {}^2\Pi_{3/2}$. These figures show that both of these two transitions have vibrational progressions. The vibrational frequencies of these progressions as computed with the CASPT2 methods are 264 and 278 cm^{-1}. These vibrational frequencies are even smaller than that of the $^3\Sigma^- \rightarrow {}^2\Pi_{1/2}$ and $^3\Sigma^- \rightarrow {}^2\Pi_{3/2}$ transitions within $AuSi^{-/0}$ (395 and 386 cm^{-1}). Such frequencies are too small to be resolved in the 532 nm photoelectron spectrum. In the 532 nm photoelectron spectrum, the X_1 and X_2 features are observed as two broad peaks. Similar to $AuSi^{-/0}$, the vibrational progressions in the $^3\Sigma^- \rightarrow {}^2\Pi_{1/2}$ and $^3\Sigma^- \rightarrow {}^2\Pi_{3/2}$ transitions within $AuGe^{-/0}$ are the results of the removal of one electron from a slightly antibonding $13b_2$ (π) orbital. In the $^3\Sigma^- \rightarrow {}^2\Pi_{1/2}$ and $^3\Sigma^- \rightarrow {}^2\Pi_{3/2}$ transitions, the Au−Ge distance is reduced from 2.378 to 2.320 Å and to 2.337 Å.

5. DISCUSSION

The emission spectra of AuSi and AuGe were reported by Barrow et al. in 1964.[28] For AuSi, the spectrum showed an A-$X_1(^2\Pi_{1/2})$ and a $X_2(^2\Pi_{3/2})$-$X_1(^2\Pi_{1/2})$ transition with transition energies of 13632 and 1071 cm^{-1}, respectively. For AuGe, the transition energies of A-$X_1(^2\Pi_{1/2})$ and $X_2(^2\Pi_{3/2})$-$X_1(^2\Pi_{1/2})$ increased to 13740 and 1552 cm^{-1}. The emission spectra of AuSi and AuGe were reinvestigated by Houdart and Schamps in 1973.[29] The transition energies were almost the same as observed by Barrow but the emission band was reassigned to

DOI: 10.1021/acs.jpca.8b01366
J. Phys. Chem. A 2018, 122, 3374−3382

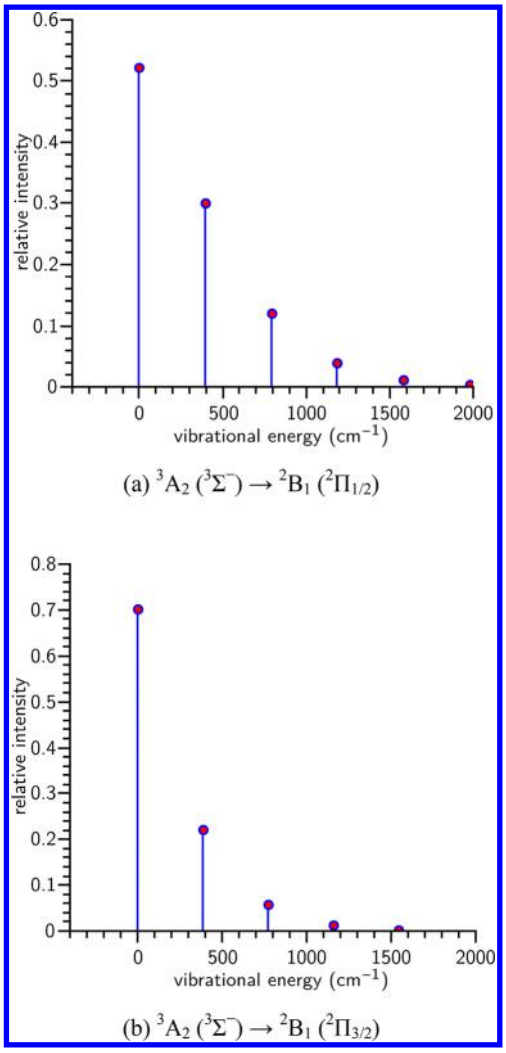

Figure 6. Franck–Condon factor simulations for the $^3A_2$ ($^3\Sigma^-$) → $^2B_1$ ($^2\Pi_{1/2}$) (a) and $^3A_2$ ($^3\Sigma^-$) → $^2B_1$ ($^2\Pi_{3/2}$) (b) transitions within the $AuSi^{-/0}$ clusters.

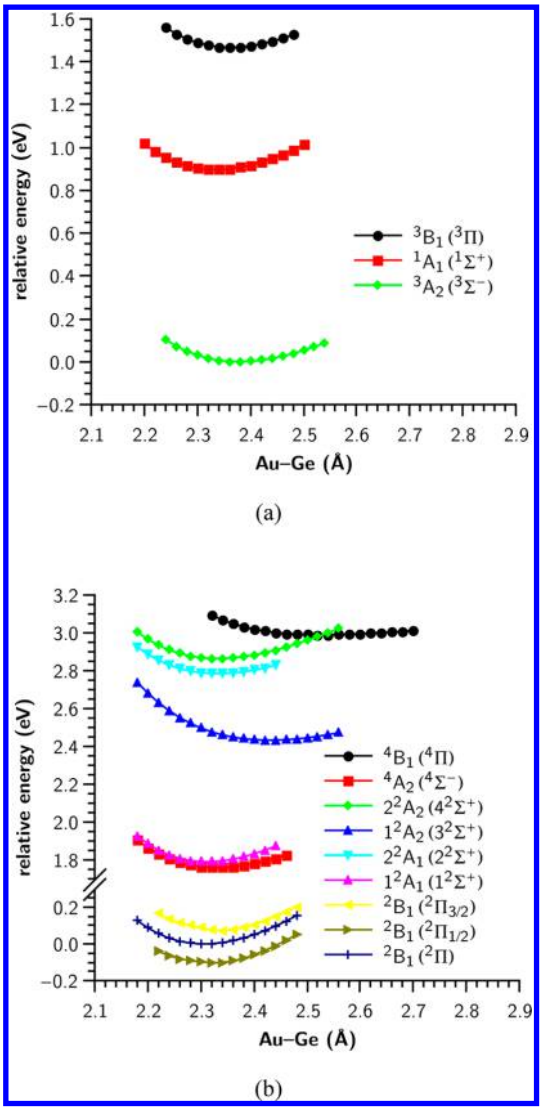

Figure 7. Potential energy curves of the low-lying states of $AuGe^-$ (a) and of AuGe (b) as obtained from CASPT2 calculations.

the $A(^2\Sigma^+)$-$X_1(^2\Pi_{1/2})$ transition. In this work, from the experimental photoelectron spectra of $AuSi^-$ and $AuGe^-$ anions, the spin–orbit splitting of AuSi is measured to be 0.15 ± 0.02 eV (1210 ± 160 cm^{-1}), slightly larger than the literature value of 1071 cm^{-1}; that of AuGe is measured to be 0.21 ± 0.02 eV (1690 ± 160 cm^{-1}), also slightly larger than the literature value of 1552 cm^{-1}. The differences to the literature values are within the uncertainties of the photoelectron measurements. The 266 nm photoelectron spectrum of $AuSi^-$ shows that the $^4\Sigma^-$ (A) state of AuSi are higher than the $^2\Pi_{1/2}$ state by 1.76 ± 0.08 eV (14195 ± 640 cm^{-1}), slightly larger than the literature value of 13632 cm^{-1} by 563 ± 640 cm^{-1} which is also within the experimental uncertainty. On the basis of the 266 nm photoelectron spectrum of $AuGe^-$, the $^4\Sigma^-$ (A) state of AuGe are higher than the $^2\Pi_{1/2}$ state by 1.87 ± 0.08 (15083 ± 640 cm^{-1}), larger than the value of 13740 cm^{-1} in the literature by 1343 ± 640 cm^{-1}. The larger term energy of AuGe $^4\Sigma^-$ (A) state observed in our experiment probably is due to the bond length of $AuGe^-$ is longer than that of AuGe. Hence, the vertical photodetachment of $AuGe^-$ corresponds to the points different from the equilibrium points on the potential curves of the neutral states.

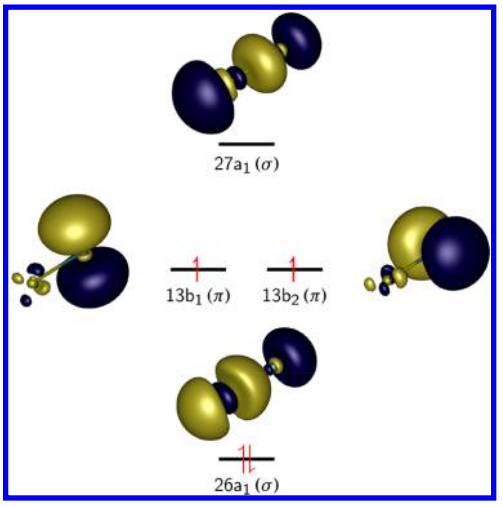

Figure 8. Qualitative molecular orbital diagram of the $^3A_2$ ($^3\Sigma^-$) of $AuGe^-$. The Au atom is placed on the left-hand side of the molecule.

By using the cavity ringdown laser absorption spectroscopy, the ground state of AuSi was defined as a $^2\Sigma$.[32] On the other

DOI: 10.1021/acs.jpca.8b01366
J. Phys. Chem. A 2018, 122, 3374–3382

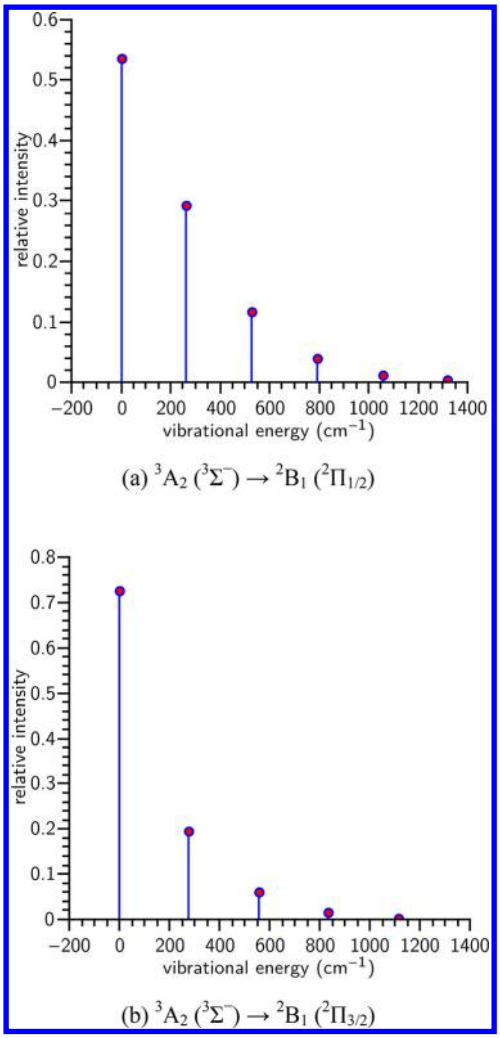

Figure 9. Franck–Condon factor simulations for the $^3A_2$ ($^3\Sigma^-$) → $^2B_1$ ($^2\Pi_{1/2}$) (a) and $^3A_2$ ($^3\Sigma^-$) → $^2B_1$ ($^2\Pi_{3/2}$) (b) transitions within the $AuGe^{-/0}$ clusters.

hand, the CASSCF/CASPT2 calculations of Abe et al. suggested the ground state of AuSi to be the $^2\Pi_{1/2}$ and the spin–orbit splitting between $^2\Pi_{1/2}$ and $^2\Pi_{3/2}$ was 1527 cm^{-1}.[33] In this work, the electronic ground states of AuSi and AuGe are calculated to be the $^2\Pi_{1/2}$. Their $^2\Pi_{1/2}$ - $^2\Pi_{3/2}$ spin–orbit splittings are calculated by theory to be 1049 and 1450 cm^{-1}, respectively. The calculated spin–orbit splittings are in good agreement with the experimental values by Barrow et al. (1071 and 1552 cm^{-1})[28] and the experimental values of this work (1210 ± 160 cm^{-1} and 1690 ± 160 cm^{-1}). In general, our CASSCF/CASPT2 calculations confirm the previous experimental and computational results for AuSi and AuGe.

As can be seen from the Franck–Condon factor simulations for the $^3\Sigma^-$ → $^2\Pi_{1/2}$ and $^3\Sigma^-$ → $^2\Pi_{3/2}$ transitions within the $AuSi^{-/0}$ and $AuGe^{-/0}$ (Figures 6 and 9), the first vibrational peaks which are the results of 0 → 0 vibrational transitions have the highest intensities. The VDEs of $AuSi^-$ and $AuGe^-$ are very similar to their ADEs. Their ADEs equal to the EAs of their neutral counterparts. Hence, the EAs of AuSi and AuGe are determined in our experiments to be 1.54 ± 0.05 eV and 1.51 ± 0.05 eV, respectively.

Also, from the photoelectron spectra, we were able to determine the term energies of the $3^2\Sigma^+$ (B) and $4^2\Sigma^+$ (C) states of AuSi and AuGe, whose values have not been reported before. The $3^2\Sigma^+$ (B) and $4^2\Sigma^+$ (C) states of AuSi are higher than the $^2\Pi_{1/2}$ state by 2.17 ± 0.08 (17502 ± 640 cm^{-1}) and 2.60 ± 0.08 eV (20970 ± 640 cm^{-1}) respectively. The $3^2\Sigma^+$ (B) and $4^2\Sigma^+$ (C) states of AuGe are higher than the $^2\Pi_{1/2}$ state by 2.17 ± 0.08 (17502 ± 640 cm^{-1}) and 2.54 ± 0.08 eV (20325 ± 640 cm^{-1}), respectively. Similar to the case of AuGe $^4\Sigma^-$ (A) state, these terms energies estimated from the anion photoelectron spectra might be slightly different from those obtained by neutral emission spectroscopy, due to the different bond lengths of $AuSi^-$ and $AuGe^-$ compared to their neutral counterparts.

6. CONCLUSIONS

We measured the photoelectron spectra of diatomic $AuSi^-$ and $AuGe^-$ and conducted calculations on the structures and electronic properties of $AuSi^{-/0}$ and $AuGe^{-/0}$. The electron affinities (EAs) of AuSi and AuGe are determined by the experiments to be 1.54 ± 0.05 eV and 1.51 ± 0.05 eV, respectively. The comparison of the theoretical results with the experimental results reveals that the electronic ground states of $AuSi^-$ and $AuGe^-$ are both a $^3\Sigma^-$ state. The photoelectron spectra of $AuSi^-$ and $AuGe^-$ can both be interpreted by the transitions from the $^3\Sigma^-$ anionic ground state to the $^2\Pi$ ($^2\Pi_{1/2}$ and $^2\Pi_{3/2}$), $^4\Sigma^-$, $3^2\Sigma^+$, and $4^2\Sigma^+$ electronic states of their neutral counterparts. The spin–orbit splitting ($^2\Pi_{1/2}$ – $^2\Pi_{3/2}$) of AuSi is measured to be 0.15 ± 0.02 eV (1210 ± 160 cm^{-1}) in agreement with the literature value of 1071 cm^{-1} and that of AuGe is measured to be 0.21 ± 0.02 eV (1690 ± 160 cm^{-1}) in agreement with the literature value of 1552 cm^{-1}. The term energy of the AuGe $^4\Sigma^-$ (A) state estimated from $AuGe^-$ photoelectron spectrum is larger than the literature value by 1343 ± 640 cm^{-1}, more likely due to the different bond lengths between $AuGe^-$ and AuGe. From the photoelectron spectra, we were able to determine the term energies of the $3^2\Sigma^+$ (B) and $4^2\Sigma^+$ (C) states of AuSi and AuGe, whose values have not been reported before. The $3^2\Sigma^+$ (B) and $4^2\Sigma^+$ (C) states of AuSi are higher than the $^2\Pi_{1/2}$ state by 2.17 ± 0.08 (17502 ± 640 cm^{-1}) and 2.60 ± 0.08 eV (20970 ± 640 cm^{-1}), respectively. The $3^2\Sigma^+$ (B) and $4^2\Sigma^+$ (C) states of AuGe are higher than the $^2\Pi_{1/2}$ state by 2.17 ± 0.08 (17502 ± 640 cm^{-1}) and 2.54 ± 0.08 eV (20325 ± 640 cm^{-1}), respectively.

■ ASSOCIATED CONTENT

Supporting Information

The Supporting Information is available free of charge on the ACS Publications website at DOI: 10.1021/acs.jpca.8b01366.

Photoelectron spectra of $AuSi^-$ and $AuGe^-$ recorded with 355 nm photons and detailed information about the subtracting spectrum of $AuSi^-$ (PDF)

■ AUTHOR INFORMATION

Corresponding Authors

*(V.T.T.) E-mail: tvtan@dthu.edu.vn.
*(J.L.) E-mail:junli@mail.tsinghua.edu.cn.
*(W.-J.Z.) E-mail: zhengwj@iccas.ac.cn.

ORCID

Van Tan Tran: 0000-0001-7878-1327
Wei-Jun Zheng: 0000-0002-9136-2693

Notes

The authors declare no competing financial interest.

DOI: 10.1021/acs.jpca.8b01366
J. Phys. Chem. A 2018, 122, 3374–3382

■ ACKNOWLEDGMENTS

This research is funded by the Vietnam National Foundation for Science and Technology Development (NAFOSTED) under Grant Number 104.06-2016.16, the National Natural Science Foundation of China (Grant Nos. 21273246 and 21103202), and the Chinese Academy of Sciences (Grant No. QYZDB-SSW-SLH024).

■ REFERENCES

(1) Madras, P.; Dailey, E.; Drucker, J. Spreading of Liquid AuSi on Vapor-Liquid-Solid-Grown Si Nanowires. *Nano Lett.* **2010**, *10*, 1759−1763.
(2) Dailey, E.; Madras, P.; Drucker, J. Au on Vapor-Liquid-Solid Grown Si Nanowires: Spreading of Liquid AuSi from the Catalytic Seed. *J. Appl. Phys.* **2010**, *108*, 064320.
(3) Matthews, T. S.; Sawyer, C.; Ogletree, D. F.; Liliental-Weber, Z.; Chrzan, D. C.; Wu, J. Q. Large Reaction Rate Enhancement in Formation of Ultrathin AuSi Eutectic Layers. *Phys. Rev. Lett.* **2012**, *108*, 096102.
(4) Berlicki, T. M.; Murawski, E.; Muszynski, M.; Osadnik, S. J.; Prociow, E. L. Thin-Film Thermocouples of Ge Doped with Au and B. *Sens. Actuators, A* **1995**, *50*, 183−186.
(5) Wood, R. A. Gold Doped Germanium as an Infrared HighFrequency Photodetector. *J. Appl. Phys.* **1965**, *36*, 1490−1491.
(6) Wang, X. X.; Getaneh, M.; Martoff, C. J.; Kaczanowicz, E. Hot Electron Effects and Dynamic Behavior of Gold Doped Germanium Thin Films as Cryogenic Phonon Sensors. *J. Appl. Phys.* **1999**, *85*, 8274−8280.
(7) Dávila, M. E.; Xian, L.; Cahangirov, S.; Rubio, A.; Le Lay, G. Germanene: a Novel Two-Dimensional Germanium Allotrope Akin to Graphene and Silicene. *New J. Phys.* **2014**, *16*, 095002.
(8) Zavodinsky, V. G.; Kuyanov, I. A. Schottky Barrier Formation in a Au/Si Nanoscale System: A Local Density Approximation Study. *J. Appl. Phys.* **1997**, *81*, 2715−2719.
(9) Sen, P.; Mitas, L. Electronic Structure and Ground states of Transition Metals Encapsulated in a Si_{12} Hexagonal Prism Cage. *Phys. Rev. B: Condens. Matter Mater. Phys.* **2003**, *68*, 155404.
(10) Chuang, F. C.; Hsu, C. C.; Hsieh, Y. Y.; Albao, M. A. Atomic and Electronic Structures of $AuSi_n$ (n = 1−16) Clusters: a First-Principles Study. *Chin. J. Phys.* **2010**, *48*, 82−102.
(11) Wang, J.; Liu, Y.; Li, Y. C. Au@Si_n: Growth Behavior, Stability and Electronic Structure. *Phys. Lett. A* **2010**, *374*, 2736−2742.
(12) Turski, P.; Barysz, M. Electronic States of the Copper, Silver, and Gold Silicides and Their Ions. *J. Chem. Phys.* **2000**, *113*, 4654−4661.
(13) Li, X.-J.; Su, K.-H. Structure, Stability and Electronic Property of the Gold-Doped Germanium Clusters: $AuGe_n$ (n = 2−13). *Theor. Chem. Acc.* **2009**, *124*, 345−354.
(14) Tai, T. B.; Nguyen, M. T. Enhanced Stability by Three-Dimensional Aromaticity of Endohedrally Doped Clusters $X_{10}M^{0/-}$ with X = Ge, Sn, Pb and M = Cu, Ag, Au. *J. Phys. Chem. A* **2011**, *115*, 9993−9999.
(15) Li, X.-J.; Ren, H.-J.; Yang, L.-M. An Investigation of Electronic Structure and Aromaticity in Medium-Sized Nanoclusters of Gold-Doped Germanium. *J. Nanomater.* **2012**, *2012*, 1−8.
(16) Li, X.; Su, K.; Yang, X.; Song, L.; Yang, L. Size-Selective Effects in the Geometry and Electronic Property of Bimetallic Au-Ge Nanoclusters. *Comput. Theor. Chem.* **2013**, *1010*, 32−37.
(17) Goicoechea, J. M.; McGrady, J. E. On the Structural Landscape in Endohedral Silicon and Germanium Clusters, M@Si_{12} and M@Ge_{12}. *Dalton Trans.* **2015**, *44*, 6755−6766.
(18) McDermott, D.; Newman, K. E. Wade's Rules and the Stability of Au_nGe_m Clusters. *Eur. Phys. J. D* **2015**, *69*, 90.
(19) Li, Y. J.; Lyon, J. T.; Woodham, A. P.; Lievens, P.; Fielicke, A.; Janssens, E. Structural Identification of Gold-Doped Silicon Clusters via Far-Infrared Spectroscopy. *J. Phys. Chem. C* **2015**, *119*, 10896−10903.
(20) Kiran, B.; Li, X.; Zhai, H. J.; Cui, L. F.; Wang, L. S. [$SiAu_4$]: Aurosilane. *Angew. Chem., Int. Ed.* **2004**, *43*, 2125−2129.
(21) Li, X.; Kiran, B.; Wang, L.-S. Gold as Hydrogen. An Experimental and Theoretical Study of the Structures and Bonding in Disilicon Gold Clusters $Si_2Au_n^-$ and Si_2Au_n (n = 2 and 4) and Comparisons to Si_2H_2 and Si_2H_4. *J. Phys. Chem. A* **2005**, *109*, 4366−4374.
(22) Kiran, B.; Li, X.; Zhai, H. J.; Wang, L. S. Gold as Hydrogen: Structural and Electronic Properties and Chemical Bonding in $Si_3Au_3^{+/0/-}$ and Comparisons to $Si_3H_3^{+/0/-}$. *J. Chem. Phys.* **2006**, *125*, 133204.
(23) Lu, S.-J.; Xu, X.-L.; Feng, G.; Xu, H.-G.; Zheng, W.-J. Structural and Electronic Properties of $AuSi_n^-$ (n = 4−12) Clusters: Photoelectron Spectroscopy and Ab Initio Calculations. *J. Phys. Chem. C* **2016**, *120*, 25628−25637.
(24) Lu, S. J.; Hu, L. R.; Xu, X. L.; Xu, H. G.; Chen, H.; Zheng, W. J. Transition from Exohedral to Endohedral Structures of $AuGe_n^-$(n = 2−12) Clusters: Photoelectron Spectroscopy and Ab Initio Calculations. *Phys. Chem. Chem. Phys.* **2016**, *18*, 20321−20329.
(25) Spiekermann, A.; Hoffmann, S.; Kraus, F.; Fassler, T. F. $[Au_3Ge_{18}]_5^-$ A Gold-Germanium Cluster with Remarkable Au-Au Interactions. *Angew. Chem., Int. Ed.* **2007**, *46*, 1638−1640.
(26) Schenk, C.; Schnepf, A. [$AuGe_{18}\{Si(SiMe_3)_3\}_6$]: A Soluble Au-Ge Cluster on the Way to a Molecular Cable? *Angew. Chem., Int. Ed.* **2007**, *46*, 5314−5316.
(27) Spiekermann, A.; Hoffmann, S. D.; Fassler, T. F.; Krossing, I.; Preiss, U. $[Au_3Ge_{45}]_9^-$ - a Binary Anion Containing a $\{Ge_{45}\}$ Cluster. *Angew. Chem., Int. Ed.* **2007**, *46*, 5310−5313.
(28) Barrow, R. F.; Gissane, W. J. M.; Travis, D. N. ELectronic Spectra of some Gaseous Diatomic Compounds of Gold. *Nature* **1964**, *201*, 603−604.
(29) Houdart, R.; Schamps, J. The Emission Spectra of the AuSi, AuGe, AuSn and AuPb Radicals. *J. Phys. B: At. Mol. Phys.* **1973**, *6*, 2478−2483.
(30) Gingerich, K. A. Gaseous Metal Silicides. I. Dissociation Energy of the Molecule AuSi. *J. Chem. Phys.* **1969**, *50*, 5426−5428.
(31) Coquant, C.; Houdart, R. Rotational Analysis of Au-Ca and Au-Si Radicals for Near Infrared Bands. *C. R. Acad. Sci. Paris* **1977**, *284*, 171−172.
(32) Scherer, J. J.; Paul, J. B.; Collier, C. P.; O'Keefe, A.; Saykally, R. J. Cavity Ringdown Laser Absorption Spectroscopy and Time-of-Flight Mass Spectroscopy of Jet-Cooled Gold Silicides. *J. Chem. Phys.* **1995**, *103*, 9187−9192.
(33) Abe, M.; Nakajima, T.; Hirao, K. A Theoretical Study of the Low-Lying States of the AuSi Molecule: an Assignment of the Excited a and d States. *J. Chem. Phys.* **2002**, *117*, 7960−7967.
(34) Xu, H.-G.; Zhang, Z.-G.; Feng, Y.; Yuan, J. Y.; Zhao, Y. C.; Zheng, W. J. Vanadium-Doped Small Silicon Clusters: Photoelectron Spectroscopy and Density-Functional Calculations. *Chem. Phys. Lett.* **2010**, *487*, 204−208.
(35) Fonseca Guerra, C.; Snijders, J. G.; te Velde, G.; Baerends, E. J. Towards an Order-N DFT Method. *Theor. Chem. Acc.* **1998**, *99*, 391−403.
(36) Te Velde, G.; Bickelhaupt, F. M.; Baerends, E. J.; Fonseca Guerra, C.; Vangisbergen, S. J. A.; Snijders, J. G.; Ziegler, T. Chemistry with ADF. *J. Comput. Chem.* **2001**, *22*, 931−967.
(37) ADF2016.106. *SCM, Theoretical Chemistry*; Vrije Universiteit: Amsterdam, The Netherlands, http://www.scm.com 2016.
(38) Becke, A. D. A New Mixing of Hartree−Fock and Local Density-Functional Theories. *J. Chem. Phys.* **1993**, *98*, 1372−1377.
(39) Becke, A. D. Density Functional Thermochemistry. III. The Role of Exact Exchange. *J. Chem. Phys.* **1993**, *98*, 5648−5652.
(40) Lee, C.; Yang, W.; Parr, R. G. Development of the Colic-Salvetti Correlation-Energy Formular into a Functional of the Electron Density. *Phys. Rev. B: Condens. Matter Mater. Phys.* **1988**, *37*, 785−789.
(41) Stephens, P. J.; Devlin, F. J.; Chabalowski, C. F.; Frisch, M. J. Ab Initio Calculation of Vibrational Absorption and Circular Dichroism Spectra Using Density Functional Force Fields. *J. Phys. Chem.* **1994**, *98*, 11623−11627.

DOI: 10.1021/acs.jpca.8b01366
J. Phys. Chem. A 2018, 122, 3374−3382

(42) Van Lenthe, E.; Baerends, E. J. Optimized Slater-Type Basis Sets for the Elements 1−118. *J. Comput. Chem.* **2003**, *24*, 1142−1156.
(43) Roos, B. O.; Lindh, R.; Malmqvist, P.-Å.; Veryazov, V.; Widmark, P. O. New Relativistic ANO Basis Sets for Transition Metal Atoms. *J. Phys. Chem. A* **2005**, *109*, 6575−6579.
(44) Roos, B. O.; Lindh, R.; Malmqvist, P.-Å.; Veryazov, V.; Widmark, P. O. Main Group Atoms and Dimers Studied with a New Relativistic ANO Basis Set. *J. Phys. Chem. A* **2004**, *108*, 2851−2858.
(45) Reiher, M.; Wolf, A. Exact Decoupling of the Dirac Hamiltonian. I. General Theory. *J. Chem. Phys.* **2004**, *121*, 2037−2047.
(46) Reiher, M.; Wolf, A. Exact Decoupling of the Dirac Hamiltonian. II. The Generalized Douglas-Kroll-Hess Transformation up to Arbitrary Order. *J. Chem. Phys.* **2004**, *121*, 10945−10956.
(47) Ishikawa, Y.; Vilkas, M. J. Relativistic Quantum Mechanics of Many-Electron Systems. *J. Mol. Struct.: THEOCHEM* **2001**, *573*, 139−169.
(48) Aquilante, F.; Pedersen, T. B.; Lindh, R.; Roos, B. O.; Sánchez de Merás, A.; Koch, H. Accurate Ab Initio Density Fitting for Multiconfigurational Self-Consistent Field Methods. *J. Chem. Phys.* **2008**, *129*, 024113.
(49) Aquilante, F.; Malmqvist, P.-Å.; Pedersen, T. B.; Ghosh, A.; Roos, B. O. Cholesky Decomposition-Based Multiconfiguration Second-Order Perturbation Theory (CD-CASPT2): Application to the Spin-State Energetics of Co^{III}(diiminato)(NPh). *J. Chem. Theory Comput.* **2008**, *4*, 694−702.
(50) Aquilante, F.; Lindh, R.; Bondo Pedersen, T. Unbiased Auxiliary Basis Sets for Accurate Two-Electron Integral Approximations. *J. Chem. Phys.* **2007**, *127*, 114107.
(51) Heß, B. A.; Marian, C. M.; Wahlgren, U.; Gropen, O. A Mean-Field Spin-Orbit Method Applicable to Correlated Wavefunctions. *Chem. Phys. Lett.* **1996**, *251*, 365−371.
(52) Aquilante, F.; Autschbach, J.; Carlson, R. K.; Chibotaru, L. F.; Delcey, M. G.; De Vico, L.; Fdez. Galván, I.; Ferré, N.; Frutos, L. M.; Gagliardi, L.; et al. Molcas 8: New Capabilities for Multiconfigurational Quantum Chemical Calculations Across the Periodic Table. *J. Comput. Chem.* **2016**, *37*, 506−541.

DOI: 10.1021/acs.jpca.8b01366
J. Phys. Chem. A 2018, 122, 3374−3382